Astronomy & Astrophysics manuscript no. 35444
May 11, 2019

Plasma environment effects on K lines of astrophysical interest

II. Ionization potentials, K thresholds, radiative rates, and Auger widths in Ne- through He-like iron ions (Fe XVII – Fe XXV)

J. Deprince[1], M.A. Bautista[2], S. Fritzsche[3,4], J.A. García[5,6], T. Kallman[7], C. Mendoza[2], P. Palmeri[1], and P. Quinet[1,8]

[1] Physique Atomique et Astrophysique, Université de Mons – UMONS, B-7000 Mons, Belgium
[2] Department of Physics, Western Michigan University, Kalamazoo, MI 49008, USA
[3] Helmholtz Institut Jena, 07743 Jena, Germany
[4] Theoretisch Physikalisches Institut, Friedrich Schiller Universität Jena, 07743 Jena, Germany
[5] Cahill Center for Astronomy and Astrophysics, California Institute of Technology, Pasadena, CA 91125, USA
[6] Dr. Karl Remeis-Observatory and Erlangen Centre for Astroparticle Physics, Sternwartstr. 7, 96049 Bamberg, Germany
[7] NASA Goddard Space Flight Center, Code 662, Greenbelt, MD, USA
[8] IPNAS, Université de Liège, Sart Tilman, B-4000 Liège, Belgium
e-mail: Pascal.Quinet@umons.ac.be

Received ??; accepted ??

ABSTRACT

Aims. In the context of accretion disks around black holes, we estimate plasma-environment effects on the atomic parameters associated with the decay of K-vacancy states in highly charged iron ions, namely Fe XVII – Fe XXV.
Methods. Within the relativistic multiconfiguration Dirac–Fock (MCDF) framework, the electron–nucleus and electron–electron plasma screenings were approximated with a time-averaged Debye-Hückel potential.
Results. Modified ionization potentials, K thresholds, wavelengths, radiative emission rates, and Auger widths are reported for astrophysical plasmas characterized by electron temperatures and densities in the ranges 10^5–10^7 K and 10^{18}–10^{22} cm^{-3}, respectively.
Conclusions. We conclude that the high-resolution microcalorimeters on board future X-ray missions such as *XRISM* and *ATHENA* are expected to be sensitive to the lowering of the iron K edge due to the extreme plasma conditions occurring in accretion disks around compact objects.

Key words. Black hole physics – Plasmas – Atomic data – X-rays: general

1. Introduction

Accurate descriptions of K-shell atomic processes are essential in the analysis of the X-ray spectra from space telescopes such as *Chandra*, *XMM-Newton*, *Suzaku*, and *NuSTAR*. In this respect, we have been involved for the past two decades in extensive computations of the relevant atomic data for cosmic abundant elements with atomic number $Z \leq 30$; we focused on iron in particular but trace elements with odd Z were also considered (see, for example, Palmeri et al. 2002, 2003a,b, 2008, 2011, 2012, 2016; Bautista et al. 2003, 2004; Kallman et al. 2004; García et al. 2005, 2009; García, Kallman & Mushotzky 2011; Mendoza et al. 2004, 2017, 2018; Witthoeft et al. 2009, 2011; Gorczyka et al. 2013; Hasoglu et al. 2014).

This data collection has become a reference source in several atomic databases for astrophysical applications, for example, Bautista & Kallman (2001), AtomDB[1], CHIANTI (Landi et al. 2012), and uaDB[2] as well as in spectral modeling codes such as XSTAR (Kallman & Bautista 2001), CLOUDY (Ferland et al. 2013), SPEX (Kaastra et al. 1996), and ION (Netzer 1996). However, these atomic parameters have been computed neglecting plasma-embedding effects, and consequently, they are not expected to be applicable at relatively high electron densities, say $n_e > 10^{18}$ cm^{-3} (Smith & Brickhouse 2014).

Absorption and emission of high-energy photons in dense plasmas occur in a wide range of astrophysical phenomena; among the most exciting perhaps are the X-rays produced and reprocessed in the regions close to compact objects such as black holes and neutron stars. In these systems the gas inflow caused by the strong gravitational potential forms an accretion disk from which copious X-ray radiation is emitted (e.g., Krolik 1999; Done et al. 2007). Observed spectra are usually imprinted with atomic features, both in emission and absorption, from a wide variety of ionic species, the modeling of which provides reliable insights of the composition, temperature, and degree of ionization of the plasma (Ross & Fabian 2005; García & Kallman 2010). In the case of a black hole, its angular momentum can be inferred by modeling the distortion of the Fe K emission complex caused by the strong relativistic effects (e.g., Reynolds 2013; García et al. 2014).

X-ray emission lines from accreting sources, in particular the Kα and Kβ lines from Fe ions, are characterized by observed widths and shifts mostly implying an origin close to the compact object (Reynolds & Nowak 2003); that is, the innermost stable circular orbit in the case of a black hole or the stellar surface in the case of a neutron star. Line intensities may thus provide estimates of key properties of these exotic dense-plasma

[1] http://www.atomdb.org
[2] http://heasarc.gsfc.nasa.gov/uadb/

Article published by EDP Sciences, to be cited as https://doi.org/10.1051/0004-6361/201935444

environments, including the effects of both special and general relativity in the emitting region that are not attainable through other observational windows. In order to analyze the Kα and Kβ emission lines to derive, for instance, the Fe ionic fractions and abundance, it is of paramount importance to rely on accurate radiative and Auger data to infer the emission and absorption rates under various extreme conditions.

Dynamical models of black-hole accretion flows appear to support densities as high as 10^{21}–10^{22} cm^{-3} (Reis & Miller 2013; Schnittman et al. 2013; Tomsick et al. 2018; Jiang et al. 2019), but thus far their effect on line emission has not been studied in detail. It is worth noting that iron-ion survival near a black hole requires such high densities to counteract the strong ionization. Therefore, plasma embedding effects on the ionic structure, K photoexcitation, and photoionization, and both radiative and Auger decay become unavoidable issues.

Following previous work on the oxygen isonuclear sequence by Deprince et al. (2019a), we estimated density effects on the atomic parameters associated with the K-vacancy states of highly charged iron ions. Multiconfiguration Dirac–Fock computations have been carried out for these species representing the plasma electron–nucleus and electron–electron shieldings with a time-averaged Debye-Hückel potential. Deprince et al. (2019a) have shown that both of these plasma interactions must be taken into account. We use a combination of the GRASP92 code (Parpia et al. 1996) to obtain the wave functions and RATIP (Fritzsche 2012) to calculate the atomic parameters. We report a first set of results on the ionization potentials (IPs), K thresholds, transition wavelengths, radiative emission rates, and Auger widths for nine ions: from Fe XVII (Ne-like) to Fe XXV (He-like).

2. Theoretical model

2.1. Relativistic multiconfiguration Dirac–Fock method

Wave functions for the ionic species Fe XVII – Fe XXV are obtained using the fully relativistic multiconfiguration Dirac–Fock (MCDF) method, implemented in the GRASP92 version (Parpia et al. 1996) of the General-purpose Relativistic Atomic Structure Program (GRASP) initially developed by Grant et al. (1980), McKenzie et al. (1980), and Grant (1988). In this approach the atomic state functions (ASF) $\Psi(\gamma J M_J)$ are expanded in linear combinations of the configuration state functions (CSF) $\Phi(\alpha_i J M_J)$

$$\Psi(\gamma J M_J) = \sum_i c_i \Phi(\alpha_i J M_J) \, . \tag{1}$$

The CSF are in turn taken as linear combinations of Slater determinants constructed from monoelectronic spin-orbitals of the form

$$\varphi_{n\kappa m}(r,\theta,\phi) = \frac{1}{r} \begin{pmatrix} P_{n\kappa}(r)\chi_{\kappa m}(\theta,\phi) \\ iQ_{n\kappa}(r)\chi_{-\kappa m}(\theta,\phi) \end{pmatrix} , \tag{2}$$

where $P_{n\kappa}(r)$ and $Q_{n\kappa}(r)$ are the large and small components of the radial wave function, respectively, and the angular functions $\chi_{\kappa m}(\theta,\phi)$ are spinor spherical harmonics. The α_i coefficients represent all the one-electron and intermediate quantum numbers needed to completely define the CSF, and γ is usually chosen as the α_i corresponding to the CSF with the largest weight $|c_i|^2$. The κ quantum number is given by

$$\kappa = \pm(j + 1/2) \, , \tag{3}$$

j being the electron total angular momentum. The sign before the parenthesis in Eq. (3) corresponds to the coupling relation between the electron orbital momentum l and its spin

$$l = j \pm 1/2 \, . \tag{4}$$

The angular functions $\chi_{\kappa m}(\theta,\phi)$ are spinor spherical harmonics in the lsj coupling scheme. Following Grant (2007) their expression is given by

$$\chi_{\kappa m}(\theta,\phi) = \sum_{\sigma=\pm 1/2} \langle l, m-\sigma, \frac{1}{2}, \sigma | l, \frac{1}{2}, m \rangle Y_l^{m-\sigma}(\theta,\phi)\xi_\sigma \tag{5}$$

with the two spinors

$$\xi_{\frac{1}{2}} = \begin{pmatrix} 1 \\ 0 \end{pmatrix} \qquad \text{and} \qquad \xi_{-\frac{1}{2}} = \begin{pmatrix} 0 \\ 1 \end{pmatrix} . \tag{6}$$

The radial functions $P_{n\kappa}(r)$ and $Q_{n\kappa}(r)$ are numerically represented on a logarithmic grid and are required to be orthonormal within each κ symmetry. In the MCDF variational procedure, the radial functions and expansion coefficients c_i are optimized self-consistently.

In the present work the restricted active space (RAS) method is used to obtain the MCDF expansions for each ionic system. In this method electrons are excited from prescribed reference configurations to a given active set of orbitals; that is, the RAS is built up by considering all the single and double excitations from the spectroscopic configurations, i.e., the configurations for which it is desirable to compute their properties, to the $n = 3$ configuration space. The list of reference configurations (i.e., the spectroscopic configurations) for each ionic system is specified as follows:

Fe XVII: $1s^22s^22p^6$, $1s^22s^22p^53s$, $1s^22s^22p^53p$, $1s2s^22p^63s$, $1s2s^22p^63p$
Fe XVIII: $1s^22s^22p^5$, $1s2s^22p^6$
Fe XIX: $1s^22s^22p^4$, $1s^22s2p^5$, $1s^22p^6$, $1s2s^22p^5$, $1s2s2p^6$
Fe XX: $1s^22s^22p^3$, $1s^22s2p^4$, $1s^22p^5$, $1s2s^22p^4$, $1s2s2p^5$, $1s2p^6$
Fe XXI: $1s^22s^22p^2$, $1s^22s2p^3$, $1s^22p^4$, $1s2s^22p^3$, $1s2s2p^4$, $1s2p^5$
Fe XXII: $1s^22s^22p$, $1s^22s2p^2$, $1s^22p^3$, $1s2s^22p^2$, $1s2s2p^3$, $1s2p^4$
Fe XXIII: $1s^22s^2$, $1s^22s2p$, $1s^22p^2$, $1s2s^22p$, $1s2s2p^2$, $1s2p^3$
Fe XXIV: $(1s+2s+2p)^3$
Fe XXV: $1s^2$, $1s2s$, $1s2p$

Computations are carried out with the extended average level (EAL) option optimizing a weighted trace of the Hamiltonian using level weights proportional to $(2J + 1)$, and they are completed with the inclusion of the relativistic two-body Breit interaction and the quantum electrodynamic corrections (QED) due to the self-energy and vacuum polarization. The MCDF ionic bound states generated by GRASP92 are then used in RATIP (Fritzsche 2012) to compute the atomic structure and the radiative and Auger parameters associated with K-vacancy states.

2.2. Plasma screening effects

We use a Debye-Hückel (DH) potential to model the plasma screening effects on the atomic properties, which in atomic units (a.u.) is given by

$$V^{DH}(r,\mu) = -\sum_{i=1}^{N} \frac{Ze^{-\mu r_i}}{r_i} + \sum_{i>j}^{N} \frac{e^{-\mu r_{ij}}}{r_{ij}} \, , \tag{7}$$

where N is the number of bound electrons, r_i is the distance of the ith electron from the nucleus, and r_{ij} is the distance between

the i and j electrons. The plasma screening parameter μ is the inverse of the Debye shielding length $\lambda_{\rm De}$, and can be expressed in terms of the plasma electron density n_e and temperature T_e as

$$\mu = \frac{1}{\lambda_{\rm De}} = \left(\frac{4\pi n_e}{kT_e}\right)^{1/2} . \quad (8)$$

A given value of μ is then associated with a certain type of plasma environment. For example, according to the magnetohydrodynamic simulations reported by Schnittman et al. (2013) for accreting black holes with ten solar masses and an accretion rate of 10%, the plasma conditions were estimated at $T_e = 10^5$–10^7 K and $n_e = 10^{18}$–10^{22} cm^{-3}. As shown in Table 1, this range corresponds to values of $\mu \lesssim 0.25$ a.u. for which the plasma-coupling parameter (Piel 2010)

$$\Gamma = \frac{q^2}{4\pi\epsilon_0 dkT} , \quad (9)$$

denoting the ratio of the electrostatic energy of neighboring particles to the thermal energy in the astrophysical plasma (predominantly protons and electrons), is always smaller (much smaller in most cases) than unity. This is in fact the validity condition for the statistically shielded DH potential to describe appropriately the screened Coulomb electrostatic interaction (see, for example, Saha & Fritzsche 2006; Belkhiri et al. 2015; Das et al. 2016). In Eq. (9) q is the charge of the neighboring particles separated by a typical distance $d = (3/4\pi n_e)^{1/3}$.

Table 1. Screening parameter μ (a.u.) for different electron temperatures and densities.

T_e (K) \ n_e (cm^{-3})	10^{18}	10^{19}	10^{20}	10^{21}	10^{22}
10^5	0.002	0.008	0.024	0.077	0.242
10^6	0.001	0.002	0.008	0.024	0.077
10^7	0.000	0.001	0.002	0.008	0.024

Therefore, when computing the atomic data with the RATIP code, we replace the electron–nucleus and electron–electron Coulomb interactions of the ionic system with the corresponding DH potential terms of Eq. (7) assuming values of the plasma screening parameter in the range $0 \le \mu \le 0.25$ a.u.. The applicability of this approach was recently discussed for the oxygen isonuclear sequence by Deprince et al. (2019a).

Table 2. Computed IPs (eV) for Fe xvii – Fe xxv as a function of the plasma screening parameter μ (a.u.). NIST values are also given for comparison.

Ion	NIST	$\mu = 0.0$	$\mu = 0.1$	$\mu = 0.25$
Fe xvii	1262.7(7)	1260.58	1214.75	1147.80
Fe xviii	1357.8(1.9)	1357.09	1308.56	1237.68
Fe xix	1460(3)	1459.12	1407.92	1333.09
Fe xx	1575.6(5)	1573.48	1519.58	1440.80
Fe xxi	1687(1)	1689.13	1632.53	1549.75
Fe xxii	1798.4(8)	1797.82	1738.54	1651.80
Fe xxiii	1950.4(1.8)	1950.49	1888.61	1798.43
Fe xxiv	2045.759(7)	2044.34	1979.79	1885.77
Fe xxv	8828.1875(11)	8836.74	8768.90	8667.86

3. Results and discussion

3.1. Ionization potentials and K thresholds

The IP and K thresholds we computed with screening parameters in the range $0 \le \mu \le 0.25$ a.u. are summarized in Tables 2–3. For the isolated ions ($\mu = 0$) we reproduce the IPs listed in the spectroscopic database of the National Institute of Standards and Technology (NIST, Kramida et al. 2018) to an accuracy better than 0.2%. The inclusion of the DH potential leads to reductions of the IP and K-threshold energy positions that increase with μ; namely 3% and 8% for $\mu = 0.10$ and $\mu = 0.25$, respectively, except for Fe xxv for which the reduction is less than 2% as a consequence of its large IP > 8600 eV. For the same reason, the K-threshold reductions are only marginal (< 2%).

Table 3. Computed K thresholds (eV) for Fe xvii – Fe xxv as a function of the plasma screening parameter μ (a.u.).

Ion	$\mu = 0.0$	$\mu = 0.1$	$\mu = 0.25$
Fe xvii	7697.64	7651.45	7582.46
Fe xviii	7827.06	7778.17	7705.19
Fe xix	7959.86	7908.27	7831.30
Fe xx	8095.41	8041.11	7960.14
Fe xxi	8246.57	8189.56	8104.56
Fe xxii	8398.74	8339.03	8250.02
Fe xxiii	8558.75	8496.29	8403.31
Fe xxiv	8689.49	8624.26	8527.21
Fe xxv	8836.74	8768.90	8667.86

This threshold lowering is a well-known phenomenon in dense-plasma physics, whose behavior is further illustrated in Figs. 1–2. For each of the ionic species considered, the DH potential predicts a linear decrease of the IP downshift with μ at a gradient that grows with ionic charge (see Fig. 1); however, as shown in Fig. 2, the IP-shift variation with effective ionic charge $Z_{\rm eff} = Z - N + 1$ for a particular μ is only moderate, i.e., ∼30%. On the other hand, we find that, for any specific ionic species, the IP and K-threshold energy shifts are practically the same (see Fig. 2).

It is interesting to highlight the fact that the inclusion of the electron–electron Debye screening effect in our calculations, in addition to that of the electron–nucleus, leads as shown in Table 4 to a substantially less pronounced IP lowering, i.e., 4% in Fe xxv to 50% in Fe xvii. This was also underlined in our previous study on the oxygen isonuclear sequence (Deprince et al. 2019a). As expected, this discrepancy grows inversely with $Z_{\rm eff}$ as the number of interacting electron–electron pairs is larger for the low-charge states.

The importance of the screening effects by the electron–electron pair interactions has also been recently brought to the fore by Das et al. (2016), who found significant influence of such effects on the IP lowering and excitation energies in Al ions, in particular in the neutral and lowly ionized species. They also found that more stable atomic systems are predicted when the electron–electron screening is taken into account, i.e., giving rise to larger IPs than those computed using a DH potential excluding the screening of the electron–electron interaction. The Debye electron–nucleus and electron–electron screening effects have been amply discussed by, for instance, Winkler (1996), Kar & Ho (2004, 2005), Saha & Fritzsche (2006), Xie et al. (2012), Certik & Winkler (2013), Jiao & Ho (2014), and Deprince et al. (2019a).

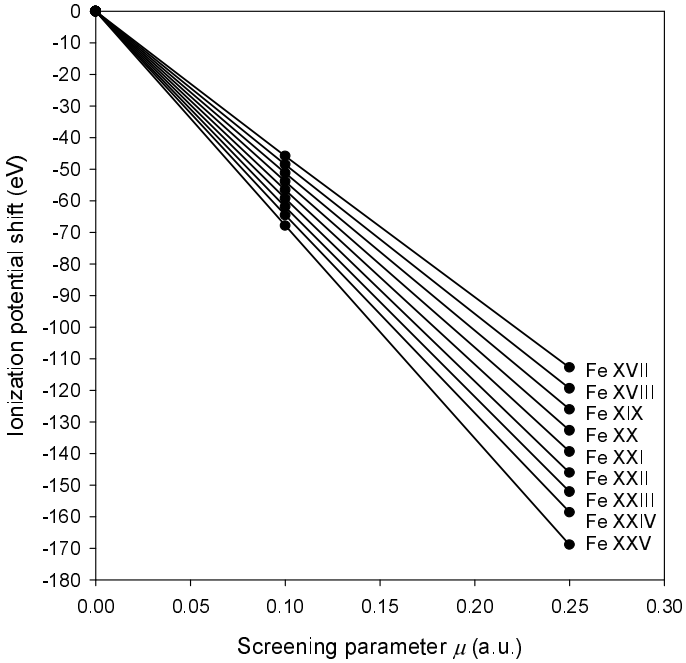

Fig. 1. Ionization potential shifts in Fe xvii – Fe xxv as a function of the plasma screening parameter μ.

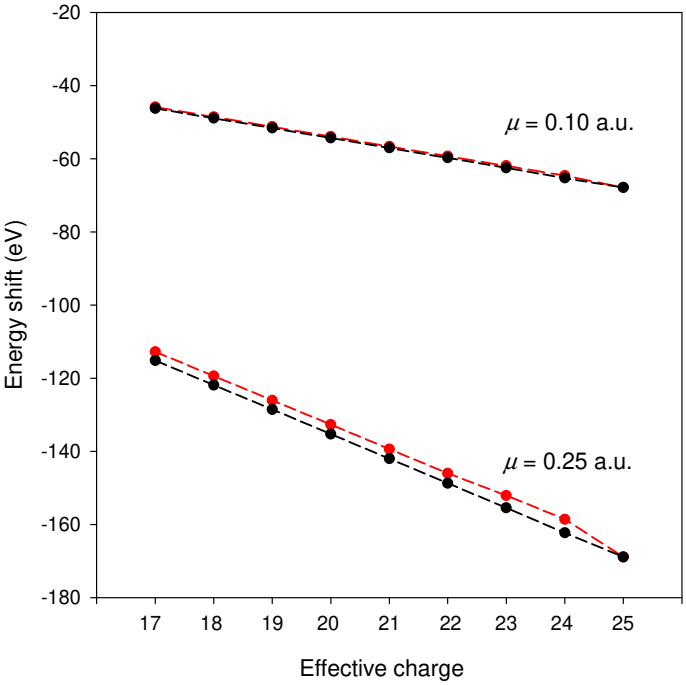

Fig. 2. Ionization potentials (black points) and K-threshold (red points) energy shifts in Fe ions as a function of effective charge $Z_{\rm eff}$ for μ = 0.1 a.u. and μ = 0.25 a.u.

3.2. Radiative transitions

Computed wavelengths and transition probabilities for the stronger K lines ($A > 10^{13}$ s^{-1}) of Fe xvii – Fe xxv with the three plasma screening parameters μ = 0.0, 0.1, and 0.25 a.u. are listed in Table 5. If our data for the isolated ion (μ = 0) are compared with Palmeri et al. (2003a) and Mendoza et al. (2004), who used the pseudo-relativistic Hartree–Fock (HFR) method, good agreement is generally found. For the transitions listed in Table 5, the wavelengths agree to better than 0.1% while the transition probabilities can show differences at the 25% level. Since we took into account similar configuration-interaction effects in our atomic models as Palmeri et al. (2003a) and Mendoza et al. (2004), the main discrepancy source must be attributed to relativistic effects, which are formally treated in the MCDF method. Furthermore, we find excellent agreement (within 5%) among our A-values computed in the Babushkin and Coulomb gauges, although only transition probabilities obtained in the Babushkin gauge are reported in Table 5.

Table 4. Ionization potentials (eV) for Fe xvii – Fe xxv computed with the DH nucleus–electron screening and with and without the electron–electron screening. The parameters μ_{ne} and μ_{ee} correspond to the screening parameter μ (a.u.) used in the first and second terms of Eq. (7), respectively. This comparison brings out the importance of the electron–electron screening.

Ion	μ_{ne} = 0.1 μ_{ee} = 0.0	μ_{ne} = 0.1 μ_{ee} = 0.1	μ_{ne} = 0.25 μ_{ee} = 0.0	μ_{ne} = 0.25 μ_{ee} = 0.25
Fe xvii	1190.72	1214.75	1089.22	1147.80
Fe xviii	1287.21	1308.56	1185.55	1237.68
Fe xix	1389.10	1407.92	1287.41	1333.09
Fe xx	1503.54	1519.58	1401.59	1440.80
Fe xxi	1619.15	1632.53	1517.02	1549.75
Fe xxii	1727.82	1738.54	1625.57	1651.80
Fe xxiii	1880.58	1888.61	1778.76	1798.43
Fe xxiv	1974.41	1979.79	1872.58	1885.77
Fe xxv	8766.28	8768.90	8661.14	8667.86

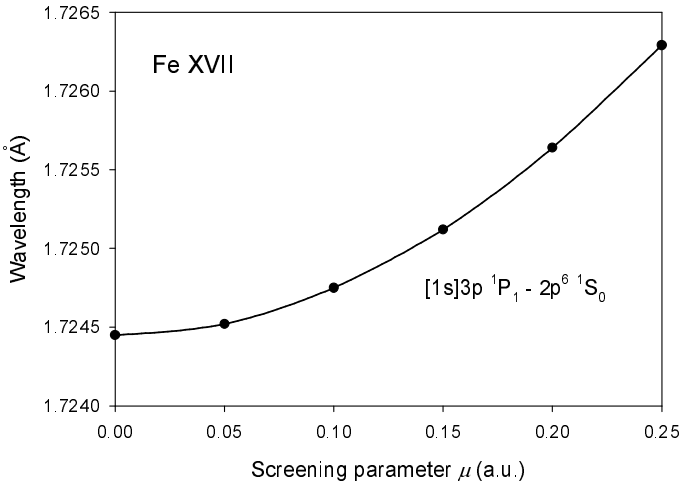

Fig. 3. Wavelength reddening as a function of the plasma screening parameter μ for the [1s]3p ^{1}P$_1$ - 2p^6 ^{1}S$_0$ Kβ line in Fe xvii.

A close inspection of Table 5 brings out the meager effects of the plasma environment on the K-line radiative parameters. For screening parameters μ = 0.10 and μ = 0.25, wavelengths appear redshifted relative to those of the isolated ion by less than 0.1 mÅ and 1 mÅ, respectively, while the variations of the radiative decay rates do not exceed more than a few percent. To illustrate this point we show in Fig. 3 the reddening of the [1s]3p ^{1}P$_1$ - 2p^6 ^{1}S$_0$ Kβ line in Fe xvii, which for μ = 0.25 amounts to ~2 mÅ. Similarly, for the [1s]2p^4 ^{2}D$_{3/2}$ - 2p^3 ^{2}D$_{3/2}$ and [1s]2p^4 ^{2}S$_{1/2}$ - 2p^3 ^{2}P$_{3/2}$ Kα lines in Fe xx in Fig. 4, the reddening is less than 1 mÅ.

It is shown in Fig. 5 for the [1s]3p ^{3}P$_0$ - [2p]3p ^{3}S$_1$ and [1s]3p ^{1}P$_1$ - 2p^6 ^{1}S$_0$ lines in Fe xvii that the plasma effects on the radiative transition probabilities (A-values) are less than 1%, although

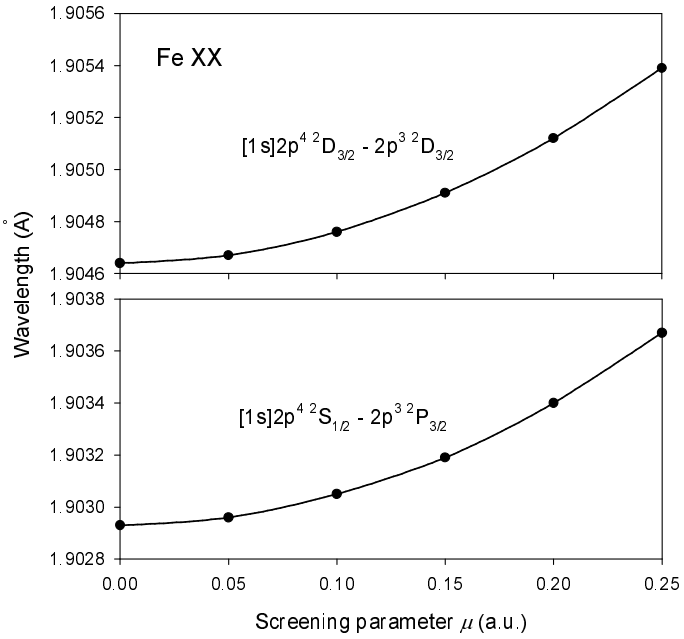

Fig. 4. Wavelength reddening as a function of the plasma screening parameter μ for the [1s]2p^4 ^{2}D$_{3/2}$ - 2p^3 ^{2}D$_{3/2}$ and [1s]2p^4 ^{2}S$_{1/2}$ - 2p^3 ^{2}P$_{3/2}$ K$_\alpha$ lines in Fe xx.

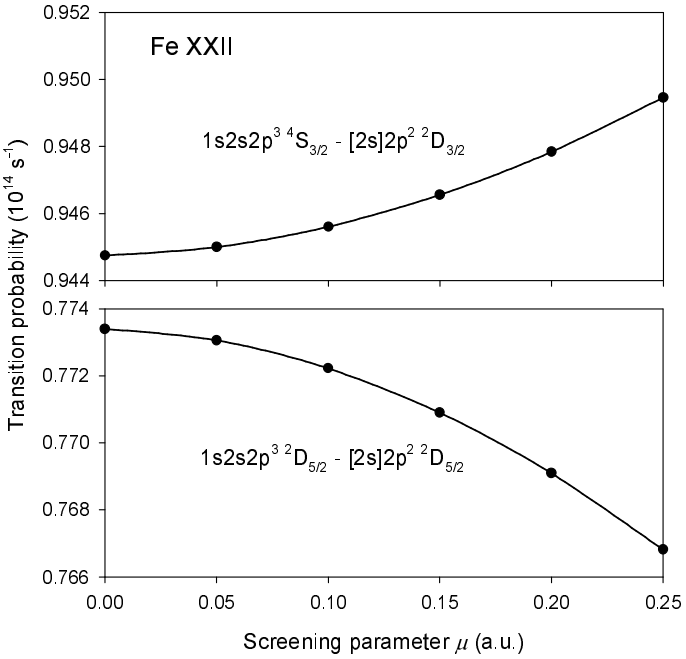

Fig. 6. Variation of the transition probability (*A*-value) with the plasma screening parameter μ for the 1s2s2p^3 ^{4}S$_{3/2}$ - [2s]2p^2 ^{2}D$_{3/2}$ and 1s2s2p^3 ^{2}D$_{5/2}$ - [2s]2p^2 ^{2}D$_{5/2}$ lines in Fe xxii.

they can increase or decrease their nominal values (μ = 0). In Fe xxii the changes are somewhat larger (3%) as illustrated in Fig. 6 with the 1s2s2p^3 ^{4}S$_{3/2}$ - [2s]2p^2 ^{2}D$_{3/2}$ and 1s2s2p^3 ^{2}D$_{5/2}$ - [2s]2p^2 ^{2}D$_{5/2}$ lines.

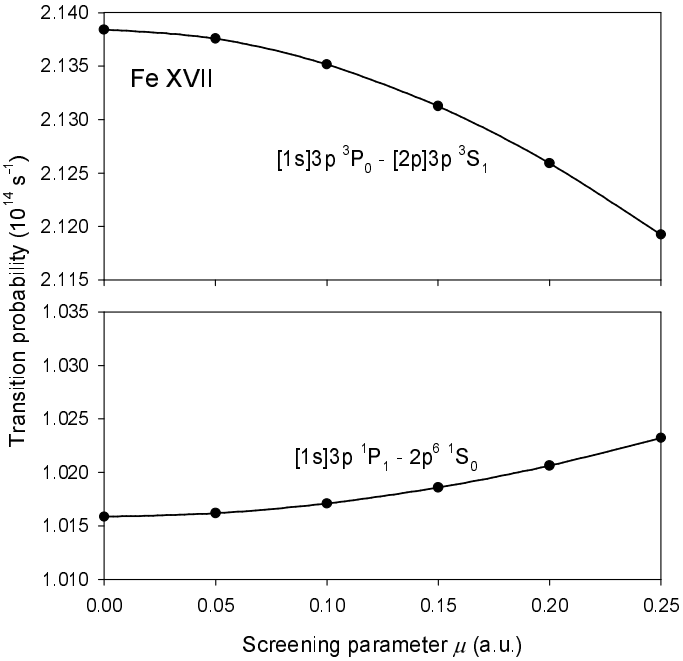

Fig. 5. Variation of the radiative transition probability (*A*-value) with the plasma screening parameter μ for the [1s]3p ^{3}P$_0$ - [2p]3p ^{3}S$_1$ and [1s]3p ^{1}P$_1$ - 2p^6 ^{1}S$_0$ lines in Fe xvii.

3.3. Auger widths

Computed Auger widths for the K-vacancy levels with screening parameters μ = 0, 0.1, and 0.25 a.u. are tabulated in Table 6. Present widths for the isolated ion case (μ = 0 a.u.) are found to be in good agreement (within 5%) with those computed previously with HFR by Palmeri et al. (2003a). The DH potential leads to more noticeable decrements of the Auger widths, namely by up to 3% and 10% for μ = 0.1 and 0.25 a.u., respectively. This variation is exemplified in Fig. 7 with the 1s2s2p^3 ^{2}D$_{3/2}$ and 1s2s^{2}2p^2 ^{4}P$_{5/2}$ K-vacancy levels in Fe xxii. We also find that the Auger widths for the higher iron ionization stages seem to be more affected by the plasma environment. As previously shown for Fe xvii, Fe xviii, and Fe xix by Deprince et al. (2019b) because of the weak variations of both the radiative rates and Auger widths with μ, the K-line fluorescence yields in the iron ions considered herein are hardly affected (3% at most).

4. Astrophysical implications

The atomic calculations hereby presented are expected to influence plasma modeling predictions in environments in which the density and temperature of the gas are such that the screening parameter μ becomes important; i.e., as shown in Table 1, for relatively low temperatures (T_e < 10^5 K) and high densities (ne_e > 10^{18} cm^{-3}). These conditions are encountered in astrophysical environments such as the solar interior (near the convective zone) or in the inner-most regions of accretion disks around compact objects (white dwarfs, neutron stars, and black holes).

Regarding plasma embedding effects in the solar interior, Krief et al. (2018) have used the ion–ion correlation model of Rozsnyai (1991, 1992) to re-evaluate the Fe Rosseland mean opacity in conditions similar to the base of the convection zone and have found a 15% increase. However, a more recent calculation (Ovechkin et al. 2019) based on the Starrett–Saumon average-atom model has questioned this result as an overestimate due to a limited treatment of the ion–ion repulsion, which is one of the points we have emphasized in the present work.

While the inclusion of the DH potential has a very small effect on the energy levels, radiative probabilities, and Auger

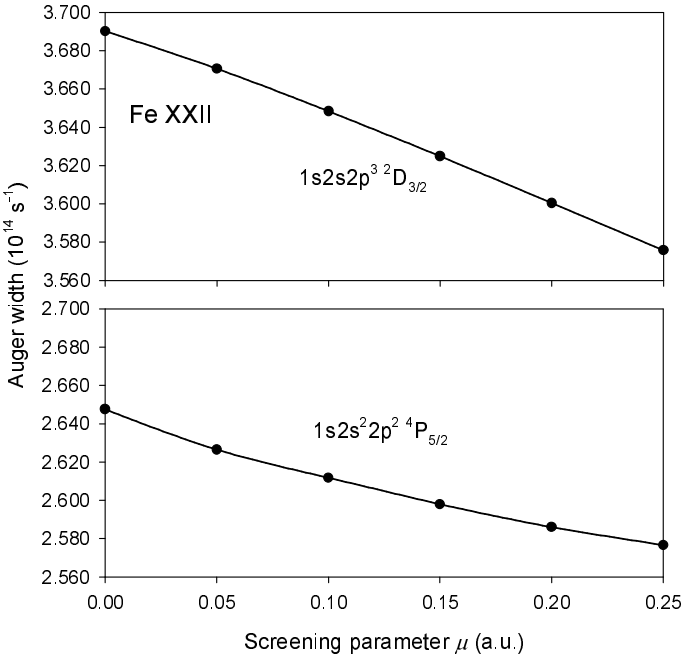

Fig. 7. Variation of the Auger width with the plasma screening parameter μ for two K-vacancy levels in Fe XXII.

widths, it does shift the IP and K threshold of each ion to lower energies. This effect would modify the part of the ionizing radiation field sampled by the photoionization cross section and, thus, the ionization rates in a photoionized plasma. For simplicity, if we assume a canonical radiation field in the form of an energy power law, the spectrum can be crudely represented by a power law $(h\nu)^{-\alpha}$. Therefore, for a flat spectrum in energy ($\alpha = 1$), the rates grow proportionally with the reduction of the K-threshold energy leading to a higher ionization rate; moreover, the steeper spectra the larger the change.

The emissivity of the fluorescent lines also displays the same dependence increasing the intensity of the observed lines. The heating of the gas due to direct photoionization has the weaker dependence $(h\nu)^{1-\alpha}$. However, it also couples the atomic parameters to the photoionized plasma equilibrium temperature resulting from the heating–cooling balance (which directly depends on DH screened scattering atomic data not treated in the present work) through the plasma screening parameter. Therefore, at this stage it is hard to make simple assumptions about the resulting spectra and deduced plasma parameters without carrying out careful simulations incorporating all the atomic data with a grid of plasma screening parameters in a photoionized plasma modeling code.

The shifts in the K thresholds are of ∼110−170 eV for Fe XVII – Fe XXV at the largest screening parameter considered in this work. These shifts are marginally too small to be detected with the available X-ray observatories. Nevertheless, changes in the Fe K-edge position will be resolved with new instruments such as the microcalorimeters aboard the future missions, namely, the X-ray Imaging and Spectroscopy Mission (*XRISM*) (Tashiro et al. 2018; Guainazzi & Tashiro 2018) and the Advanced Telescope for High ENergy Astrophysics (*ATHENA*) (Nandra et al. 2013; Guainazzi & Tashiro 2018), which will have a resolution of a few electronvolts. It is worth mentioning that, unlike the energies of the K thresholds, the energies of the Kα and Kβ lines are almost unaffected by high density plasma effects. Hence, high spectral resolution observations should yield information on the ionization structure of the plasma and plasma effect simultaneously. This is by constraining the presence of different ionic stages on the position and structure of the K lines, while diagnosing plasma screening effects on the position and structure of the respective K thresholds. Moreover, we emphasize that the effects mentioned in this work only concern changes in the ionic radiative properties. Other plasma effects at high densities, such as the continuum lowering and increase of the collisional rates, are expected to introduce additional modifications to the observed spectra. These effects will be a matter of further study in our ongoing projects.

5. Summary and conclusions

The influence of the plasma environment on the atomic structure and the radiative and Auger properties of K lines in highly charged iron ions (from He-like Fe XXV to Ne-like Fe XVII) has been studied by means of a time-averaged Debye–Hückel screened potential in the context of the relativistic multiconfiguration Dirac–Fock framework. The explored plasma screening-parameter space of the problem spans $0 \leq \mu \leq 0.25$ a.u. corresponding to conditions expected in compact-object accretion disks. The results can be summarized as follows:

1. The IPs and K-threshold energies are both lowered by the plasma environment. The lowering is found to be linearly dependent on both the plasma screening parameter μ and the ionic effective charge $Z_{\rm eff}$. They vary from ∼110 eV to ∼170 eV for $\mu = 0.25$ a.u. corresponding to extreme plasma conditions.
2. The importance of the electron–electron plasma screening has been reconfirmed.
3. Plasma environment effects are negligibly small on the wavelengths (redshifted by less than ∼ 0.1 Å), the transition probabilities, and the Auger widths; the transition probabilities decrease or increase, depending on transitions, by a few percent and the Auger widths decrease by at most ∼10%.

In conclusion, the high-resolution X-ray spectrometers aboard future missions such as *XRISM* and *ATHENA* are expected to be sensitive to the lowering of the iron K edge due to the extreme plasma conditions occurring in accretion disks around compact objects.

Acknowledgements. J.D. is Research Fellow of the Belgian Fund for Research Training in Industry and Agriculture (FRIA) while P.P. and P.Q. are, respectively, Research Associate and Research Director of the Belgian Fund for Scientific Research (F.R.S.-FNRS). Financial supports from these organizations, as well as from the NASA Astrophysics Research and Analysis Program (grant 80NSSC17K0345) are gratefully acknowledged. J.A.G. acknowledges support from the Alexander von Humboldt Foundation.

References

Bautista, M. A., & Kallman, T. R. 2001, ApJS, 134, 139
Bautista, M. A., Mendoza, C., Kallman, T. R., & Palmeri, P. 2003, A&A, 403, 339
Bautista, M. A., Mendoza, C., Kallman, T. R., & Palmeri, P. 2004, A&A, 418, 1171
Belkhiri, M., Fontes, C. J., & Poirier, M. 2015, Phys. Rev. A, 92, 032501
Certik, O., & Winkler, P. 2013, Int. J. Quant. Chem., 113, 2012
Das, M., Sahoo, B. K., & Pal, S., 2016, Phys. Rev. A, 93, 052513
Deprince, J., Bautista, M. A., Fritzsche, S., García, J., Kallman, T. R., Mendoza, C., Palmeri, P., & Quinet, P. 2019a, A&A, to be published
Deprince, J., Bautista, M. A., Fritzsche, S., García, J., Kallman, T. R., Mendoza, C., Palmeri, P., & Quinet, P. 2019b, X-Ray Spectrom., to be published
Done, C., Gierlinski, M., & Kubota, A. 2007, A&ARv, 15, 1

Ferland, G. J., Porter, R. L., van Hoof, P. A. M., Williams, R. J. R., Abel, N. P., Lykins, M. L., Shaw, G., Henney, W. J., & Stancil, P. C. 2013, Rev. Mex. Astron. Astrophys., 49, 137
Fritzsche, S. 2012, Comput. Phys. Commun., 183, 1523
García, J., Dauser, T., Lohfink, A., Kallman, T. R., Steiner, J. F., McClintock, J. E., Brenneman, L., Wilms, J., Eikmann, W., Reynolds, C. S., & Tombesi, F. 2014, ApJ, 782, 76
García, J., & Kallman, T. R. 2010, ApJ, 718, 695
García, J., Kallman, T. R., & Mushotzky, R. F. 2011, ApJ, 731, 131
García, J., Kallman, T. R., Witthoeft, M. C., Behar, E., Mendoza, C., Palmeri, P., Quinet, P., Bautista, M. A., & Klapisch, M. 2009, ApJS, 185, 477
García, J., Mendoza, C., Bautista, M. A., Gorczyka, T. W., Kallman, T. R., & Palmeri, P. 2005, ApJS, 158, 68
Gorczyka, T. W., Bautista, M. A., Hasoglu, M. F., García, J., Gatuzz, E. Kaastra, J. S., Kallman, T. R., Manson, S. T., Mendoza, C., Raassen, A. J. J., de Vries, C. P., & Zatsarinny, O. 2013, ApJ, 779, 78
Grant, I. P. 1988, Meth. Comput. Chem., 2, 1
Grant, I. P. 2007, Relativistic Quantum Theory of Atoms and Molecules (Springer-Verlag, New York)
Grant, I. P., McKenzie, B. J., Norrington, P. H., Mayers, D. F., & Pyper, N. C. 1980, Comput. Phys. Commun., 21, 207
Guainazzi, M., & Tashiro, M. S. 2018, arXiv e-prints, arXiv:1807.06903
Hasoglu, M. F., Abdel-Naby, S. A., Gatuzz, E., García, J., Kallman, T. R., Mendoza, C., & Gorczyka, T. W. 2014, ApJS, 214, 8
Jiang, J., Fabian, A. C., Wang, J., Walton, D. J., García J. A., Parker, M. L., Steiner, J. F., & Tomsick, J. A. 2019, MNRAS, 484, 1972
Jiao, L. G., & Ho, Y. K. 2014, J. Quant. Spectrosc. Radiat. Transf., 144, 27
Kaastra, J. S., Mewe, R., & Nieuwenhuijzen, H. 1996, in UV and X-ray Spectroscopy of Astrophysical and Laboratory Plasmas, ed. K. Yamashita & T. Watanabe, 411
Kallman, T. R., & Bautista, M. A. 2001, ApJS, 133, 221
Kallman, T. R., Palmeri, P., Bautista, M. A., Mendoza, C., & Krolik, J. H. 2004, ApJS, 155, 675
Kar, S., & Ho, Y. K. 2004, Phys. Rev. E, 70, 066411
Kar, S., & Ho, Y. K. 2005, New. J. Phys., 7, 141
Kramida, A., Ralchenko, Yu., Reader, J. and NIST ASD Team 2018, NIST Atomic Spectra Database (version 5.6.1). Available: `http://physics.nist.gov/asd` [2019, February 1]. National Institute of Standards and Technology, Gaithersburg, MD
Krief, M., Kurzweil, Y., Feigel, A., & Gazit, D., 2018, ApJ, 856, 135
Krolik, J. H. 1999, Active Galactic Nuclei from the Central Black Hole to the Galactic Environment (Princeton Univ. Press, Princeton)
Landi, E., Del Zanna, G., Young, P. R., Dere, K. P., & Mason, H. E. 2012, ApJ, 744, 99
McKenzie, B. J., Grant, I. P., & Norrington, P. H. 1980, Comput. Phys. Commun., 21, 233
Mendoza C., Bautista M. A., Palmeri P., Quinet P., Witthoeft M. C., & Kallman T. R., 2017, A&A, 604, A63
Mendoza C., Bautista M. A., Palmeri P., Quinet P., Witthoeft M. C., & Kallman T. R., 2018, A&A, 616, A62
Mendoza, C., Kallman, T. R., Bautista, M. A., & Palmeri, P. 2004, A&A, 414, 377
Nandra, K., Barret, D., Barcons, X., et al. 2013, arXiv e-prints, arXiv:1306.2307
Netzer, H. 1996, ApJ, 473, 781
Ovechkin, A. A., Loboda, P. A., & Falkov, A. L., 2019, arXiv: 1810.06027, High Energy Density Physics, submitted.
Palmeri, P., Mendoza, C., Kallman, T. R., & Bautista, M. A. 2002, ApJ, 577, L119
Palmeri, P., Mendoza, C., Kallman, T. R., & Bautista, M. A. 2003a, A&A, 403, 1175
Palmeri, P., Mendoza, C., Kallman, T. R., Bautista, M. A., & Meléndez, M. 2003b, A&A, 410, 359
Palmeri, P., Quinet, P., Mendoza, C., Bautista, M. A., García, J., & Kallman, T. R. 2008, ApJS, 177, 408
Palmeri, P., Quinet, P., Mendoza, C., Bautista, M. A., García, J., Witthoeft, M. C., & Kallman, T. R. 2011, A&A, 525, A59
Palmeri P., Quinet P., Mendoza C., Bautista M. A., García J., Witthoeft M. C., & Kallman T. R., 2012, A&A, 543, A44
Palmeri P., Quinet P., Mendoza C., Bautista M. A., Witthoeft M. C., & Kallman T. R., 2016, A&A, 589, A137
Parpia, F. A., Fischer, C. F., & Grant, I. P. 1996, Comput. Phys. Commun., 94, 249
Piel, A. 2010, Plasma Physics. An Introduction to Laboratory, Space and Fusion Plasmas (Springer Verlag, Berlin-Heidelberg)
Reis, R. C., & Miller, J. M. 2013, ApJ, 769, L7
Reynolds, C. S. 2013, Class. Quantum Grav., 30, 244004
Reynolds, C. S., & Nowak, M. A. 2003, Phys. Rep., 377, 389
Ross, R. R., & Fabian, A. C. 2005, MNRAS, 358, 211
Rozsnyai, B. F., 1992, ApJ, 393, 409
Rozsnyai, B. F., 1991, Phys. Rev. A, 43, 3035
Saha, B., & Fritzsche, S. 2006, Phys. Rev. E, 73, 036405
Schnittman, J. D., Krolik, J. H., & Noble, S. C. 2013, ApJ, 769, 156
Smith, R. K., & Brickhouse, N. S. 2014, Adv. At. Mol. Opt. Phys., 63, 271
Tashiro, M., Maejima, H., Toda, K., et al. 2018, SPIE Conf. Ser., 10699, 1069922
Tomsick, J. A., Parker, M. L, García, J. A., Yamaoka, K., Barret, D., Chiu, J.-L., Clavel, M., Fabian, A., Fürst, F., Gandhi, P., Grinberg, V., Miller, J. M., Pottschmidt, K., & Walton, D. J. 2018, ApJ, 855, 3
Winkler, P. 1996, Phys. Rev. E, 53, 5517
Witthoeft, M. C., Bautista, M. A., Mendoza, C., Kallman, T. R., Palmeri, P., & Quinet, P. 2009, ApJS, 182, 127
Witthoeft, M. C., García, J., Kallman, T. R., Bautista, M. A., Mendoza, C., Palmeri, P., & Quinet, P. 2011, ApJS, 192, 7
Xie, L. Y., Wang, J. G., Janev, R. K., Qu, Y. Z., & Dong, C. Z. 2012, Eur. Phys. J. D, 66, 125

Table 5. Comparison of wavelengths and transition probabilities for the K lines of Fe XVII – Fe XXV ($17 \leq Z_{\rm eff} \leq 25$) computed with plasma screening parameters $\mu = 0.0$, 0.1, and 0.25 a.u. Data obtained with $\mu = 0$ a.u. corresponds to an isolated ion.

$Z_{\rm eff}$	Transition	Wavelength (Å)			Transition probability (s^{-1})		
		$\mu = 0.0$	$\mu = 0.1$	$\mu = 0.25$	$\mu = 0.0$	$\mu = 0.1$	$\mu = 0.25$
17	[1s]3p $^1P_1$ – 2p^6 $^1S_0$	1.7244	1.7248	1.7263	1.016E+14	1.017E+14	1.023E+14
17	[1s]3p $^1P_1$ – [2p]3p $^3S_1$	1.9253	1.9254	1.9260	1.131E+13	1.130E+13	1.127E+13
17	[1s]3p $^3P_2$ – [2p]3p $^3S_1$	1.9263	1.9264	1.9270	2.370E+13	2.373E+13	2.386E+13
17	[1s]3p $^1P_1$ – [2p]3p $^3D_2$	1.9265	1.9267	1.9273	2.919E+13	2.927E+13	2.964E+13
17	[1s]3s $^1S_0$ – [2p]3s $^1P_1$	1.9268	1.9269	1.9275	3.225E+14	3.223E+14	3.211E+14
17	[1s]3p $^3P_1$ – [2p]3p $^3S_1$	1.9270	1.9271	1.9277	8.108E+13	8.109E+13	8.112E+13
17	[1s]3p $^3P_0$ – [2p]3p $^3S_1$	1.9272	1.9273	1.9279	2.138E+14	2.135E+14	2.119E+14
17	[1s]3p $^1P_1$ – [2p]3p $^1P_1$	1.9274	1.9275	1.9281	1.108E+14	1.107E+14	1.103E+14
17	[1s]3s $^3S_1$ – [2p]3s $^3P_2$	1.9278	1.9279	1.9285	3.401E+14	3.400E+14	3.394E+14
17	[1s]3p $^3P_2$ – [2p]3p $^3D_3$	1.9280	1.9281	1.9287	2.871E+14	2.870E+14	2.865E+14
17	[1s]3p $^1P_1$ – [2p]3p $^3P_2$	1.9280	1.9281	1.9287	1.505E+14	1.504E+14	1.497E+14
17	[1s]3p $^3P_1$ – [2p]3p $^3D_2$	1.9283	1.9284	1.9290	3.090E+14	3.088E+14	3.079E+14
17	[1s]3p $^3P_2$ – [2p]3p $^1P_1$	1.9284	1.9285	1.9291	1.453E+13	1.450E+13	1.435E+13
17	[1s]3s $^3S_1$ – [2p]3s $^1P_1$	1.9285	1.9286	1.9292	9.717E+13	9.718E+13	9.724E+13
17	[1s]3p $^3P_2$ – [2p]3p $^3P_2$	1.9290	1.9291	1.9297	9.841E+13	9.840E+13	9.834E+13
17	[1s]3p $^3P_0$ – [2p]3p $^1P_1$	1.9293	1.9294	1.9300	2.092E+14	2.094E+14	2.102E+14
17	[1s]3p $^3P_1$ – [2p]3p $^3P_2$	1.9297	1.9298	1.9304	2.434E+13	2.439E+13	2.461E+13
17	[1s]3p $^1P_1$ – [2p]3p $^3P_0$	1.9297	1.9298	1.9305	1.148E+13	1.143E+13	1.119E+13
17	[1s]3p $^1P_1$ – [2p]3p $^3D_1$	1.9302	1.9303	1.9309	3.116E+13	3.121E+13	3.145E+13
17	[1s]3s $^1S_0$ – [2p]3s $^3P_1$	1.9304	1.9305	1.9311	2.896E+14	2.896E+14	2.899E+14
17	[1s]3p $^1P_1$ – [2p]3p $^3P_1$	1.9312	1.9313	1.9319	5.188E+13	5.184E+13	5.167E+13
17	[1s]3p $^1P_1$ – [2p]3p $^3D_2$	1.9313	1.9314	1.9320	1.580E+14	1.580E+14	1.577E+14
17	[1s]3p $^3P_1$ – [2p]3p $^3P_0$	1.9315	1.9316	1.9322	5.507E+13	5.510E+13	5.523E+13
17	[1s]3s $^3S_1$ – [2p]3s $^3P_0$	1.9316	1.9317	1.9324	6.669E+13	6.667E+13	6.656E+13
17	[1s]3p $^3P_1$ – [2p]3p $^3D_1$	1.9319	1.9320	1.9327	1.099E+14	1.098E+14	1.093E+14
17	[1s]3s $^3S_1$ – [2p]3s $^3P_1$	1.9321	1.9322	1.9328	1.042E+14	1.042E+14	1.038E+14
17	[1s]3p $^3P_0$ – [2p]3p $^3D_1$	1.9321	1.9322	1.9328	1.694E+14	1.693E+14	1.689E+14
17	[1s]3p $^3P_2$ – [2p]3p $^3P_1$	1.9322	1.9323	1.9329	7.919E+13	7.915E+13	7.896E+13
17	[1s]3p $^3P_2$ – [2p]3p $^3D_2$	1.9323	1.9324	1.9331	1.014E+14	1.013E+14	1.010E+14
17	[1s]3p $^3P_0$ – [2p]3p $^3P_1$	1.9331	1.9332	1.9338	1.615E+13	1.619E+13	1.637E+13
17	[1s]3p $^1P_1$ – [2p]3p $^1S_0$	1.9380	1.9381	1.9388	4.421E+13	4.421E+13	4.421E+13
17	[1s]3p $^3P_1$ – [2p]3p $^1S_0$	1.9398	1.9399	1.9406	1.056E+13	1.051E+13	1.029E+13
18	[1s]2p^6 $^2S_{1/2}$ – 2p^5 $^2P_{3/2}$	1.9262	1.9263	1.9268	4.116E+14	4.115E+14	4.103E+14
18	[1s]2p^6 $^2S_{1/2}$ – 2p^5 $^2P_{1/2}$	1.9301	1.9302	1.9307	2.018E+14	2.017E+14	2.012E+14

Notes. A complete version of this table is available in electronic form from the CDS.

Table 6. Plasma environment effects on the Auger widths of K-vacancy states in Fe XVII – Fe XXV ($17 \leq Z_{\rm eff} \leq 25$) computed with plasma screening parameters $\mu = 0.0$, 0.1, and 0.25 a.u. Data obtained with $\mu = 0$ a.u. corresponds to an isolated ion.

$Z_{\rm eff}$	Level	Auger width (s^{-1})		
		$\mu = 0.0$	$\mu = 0.1$	$\mu = 0.25$
17	[1s]3s $^3S_1$	7.711E+14	7.647E+14	7.604E+14
17	[1s]3s $^1S_0$	8.135E+14	8.069E+14	8.027E+14
17	[1s]3p $^3P_0$	7.610E+14	7.548E+14	7.420E+14
17	[1s]3p $^3P_1$	7.302E+14	7.243E+14	7.128E+14
17	[1s]3p $^3P_2$	7.154E+14	7.097E+14	7.069E+14
17	[1s]3p $^1P_1$	7.244E+14	7.189E+14	7.106E+14
18	[1s]2p^6 $^2S_{1/2}$	1.529E+15	1.523E+15	1.504E+15
19	[1s]2p^5 $^3P_2$	8.058E+14	8.016E+14	7.951E+14
19	[1s]2p^5 $^3P_1$	7.929e+14	7.890E+14	7.828E+14
19	[1s]2p^5 $^3P_0$	7.803E+14	7.764E+14	7.699E+14
19	[1s]2p^5 $^1P_1$	7.512E+14	7.484E+14	7.427E+14
19	1s2s2p^6 $^3S_1$	7.663E+14	7.623E+14	7.598E+14
19	1s2s2p^6 $^1S_0$	1.137E+15	1.130E+15	1.115E+15

Notes. A complete version of this table is available in electronic form from the CDS.